



저작자표시-비영리-변경금지 2.0 대한민국

이용자는 아래의 조건을 따르는 경우에 한하여 자유롭게

- 이 저작물을 복제, 배포, 전송, 전시, 공연 및 방송할 수 있습니다.

다음과 같은 조건을 따라야 합니다:



저작자표시. 귀하는 원저작자를 표시하여야 합니다.



비영리. 귀하는 이 저작물을 영리 목적으로 이용할 수 없습니다.



변경금지. 귀하는 이 저작물을 개작, 변형 또는 가공할 수 없습니다.

- 귀하는, 이 저작물의 재이용이나 배포의 경우, 이 저작물에 적용된 이용허락조건을 명확하게 나타내어야 합니다.
- 저작권자로부터 별도의 허가를 받으면 이러한 조건들은 적용되지 않습니다.

저작권법에 따른 이용자의 권리는 위의 내용에 의하여 영향을 받지 않습니다.

이것은 [이용허락규약\(Legal Code\)](#)을 이해하기 쉽게 요약한 것입니다.

[Disclaimer](#)

공학석사 학위논문

**Study on Effects of Titanium  
Silicide Coating onto Porous Silicon  
Nanospheres for Lithium Ion  
Battery Anodes**

타이타늄 실리사이드가 코팅된  
다공성 실리콘 입자의 리튬이온전지  
음극소재로서의 효과 연구

2014년 8월

서울대학교 대학원  
공과대학 화학생물공학부

김 영 민

**Study on Effects of Titanium  
Silicide Coating onto Porous Silicon  
Nanospheres for Lithium Ion  
Battery Anodes**

지도 교수 성 영 은

이 논문을 공학석사 학위논문으로 제출함  
2014 년 6 월

서울대학교 대학원  
공과대학 화학생물공학부 에너지환경화학융합기술전공  
김 영 민

김영민의 석사 학위논문을 인준함  
2014 년 6 월

위 원 장 \_\_\_\_\_ (인)

부위원장 \_\_\_\_\_ (인)

위 원 \_\_\_\_\_ (인)

## **Abstract**

# **Study on Effects of Titanium Silicide Coating onto Porous Silicon Nanospheres for Lithium Ion Battery Anodes**

**김영민**

School of Chemical & Biological Engineering  
Seoul National University

Lithium ion batteries (LIBs) have been applied mainly in small-portable devices as power sources. However, the medium-large size battery sector such as electric vehicles (EVs) and energy storage system (ESS) have opened recently, and thus the demand for much higher power density, and low cost materials has been increased.. Si is considered as one of the most promising anode material for LIBs, due to its high theoretical capacity, nontoxic, low cost and abundance. On the other hand, Si anode has intrinsic limitations such as severe volume change and low electrical conductivity, which leads to poor cycling and rate performances, which severely limits their applications.

In this research, we present a facile synthesis of porous Si structure and enhancement of electrical conductivity via magnesiothermic reduction and  $\text{TiSi}_2$  coating layer, overcoming these limitations. Taking advantages of the porous structure and the high electrically conductive coating layer make this anode exhibit a significantly enhanced electrochemical performance in terms of cyclic, rate capability and charge transfer resistance. The  $\text{TiSi}_2$  is inactive toward lithium, which is negatively influenced in terms of specific capacity. Nevertheless, the  $\text{TiSi}_2$ , which has good electrical conductivity and physical strength, not only enhance the conductivity but also maintain Si structure during cycling. This combination of porous structure via magnesiothermic reduction and highly conductive  $\text{TiSi}_2$  coating makes a synergistic effect of electrochemical performance. This novel synthesis is demonstrated as promising method for producing high capacity anode materials applicable in the next generation LIBs.

**Keywords:** Lithium ion batteries, anode, silicon, magnesiothermic reduction, titanium silicide

**Student Number: 2012-23975**

## List of Figures

<b>Figure 1.1</b>	The increasing demand for high energy and power density.....	2
<b>Figure 1.2</b>	Schematic illustration of materials for cathode and anode materials.....	3
<b>Figure 1.3</b>	Silicon electrode failure mechanisms.....	5
<b>Figure 1.4</b>	Various porous silicon structure by magnesiothermic reduction.....	7
<b>Figure 3.1</b>	Schematic structure illustration of the synthesis of P-Si and P-Si@TiSi <sub>2</sub> sphere.....	20
<b>Figure 3.2</b>	XRD patterns of SiO <sub>2</sub> , P-Si, P-Si@TiSi <sub>2</sub> -1 and P-Si@TiSi <sub>2</sub> -2 spheres.....	21
<b>Figure 3.3</b>	SEM images of P-Si, P-Si@TiSi <sub>2</sub> -1, P-Si@TiSi <sub>2</sub> -2.....	24
<b>Figure 3.4</b>	EDS mapping of P-Si@TiSi <sub>2</sub> -1.....	26
<b>Figure 3.5</b>	EDS mapping of P-Si@TiSi <sub>2</sub> -2.....	27
<b>Figure 3.6</b>	TEM images of P-Si, P-Si@TiSi <sub>2</sub> -1, P-Si@TiSi <sub>2</sub> -2 .....	29
<b>Figure 3.7</b>	TEM images of before and after magnesiothermic reduction.....	30
<b>Figure 3.8</b>	EDS line scan datas of P-Si@TiSi <sub>2</sub> -1 and P-Si@TiSi <sub>2</sub> .	31
<b>Figure 3.9</b>	Nitrogen adsorption-desorption isotherms at 77.....	33

<b>Figure 3.10</b>	Cycle voltage profile at 1, 5, 10, 30, 50.....	36
<b>Figure 3.11</b>	Electrochemical performances.....	39
<b>Figure 3.12</b>	Cyclic voltammetry of P-Si, P-Si@TiSi <sub>2</sub> -1 and P-Si@TiSi <sub>2</sub> -2.....	41
<b>Figure 3.13</b>	EIS Nyquist plots of the P-Si, P-Si@TiSi <sub>2</sub> -1 and P-Si@TiSi <sub>2</sub> -2 at the lithiated state after 3 cycle.....	43
<b>Figure 3.14</b>	SEM images of before and after cycling.....	45
<b>Figure 3.15</b>	TEM images of before and after cycling.....	46

## List of Tables

Table 1. this table shows the resistivity and conductivity of various materials at 20°C.....	10
--	----

# Contents

<b>Abstract .....</b>	<b>i</b>
<b>List of Figures .....</b>	<b>iii</b>
<b>List of Tables.....</b>	<b>v</b>
<b>Contents.....</b>	<b>vi</b>
<b>Chapter 1. Introduction .....</b>	<b>1</b>
<b>Chapter 2. Expeimental .....</b>	<b>12</b>
2.1 Preparation of materials .....	12
2.2 Preparation of composite electrode .....	14
2.3 Preparation of half cell .....	14
2.4 Characterization .....	14
2.5 Electrochemical measurement .....	16
<b>Chapter 3 Results and discussion .....</b>	<b>18</b>
3.1 The analysis of powder .....	18
3.2 The electrochemical analysis .....	34
<b>Chapter 4 Conclusions .....</b>	<b>47</b>
<b>References .....</b>	<b>48</b>
<b>국문초록.....</b>	<b>53</b>

## Chapter 1. Introduction

Lithium-ion batteries (LIBs) have been used as the most dominant power sources for portable electronics, electric vehicles (EVs) and energy storage system (ESS) as shown in Figure 1.1 [1, 2]. The demands for much higher energy and power densities, low cost cathode and anode materials have been increasing. The most widely used anode is graphite due to its long cycle life, low cost and abundance in nature. However, the graphite anode already has been optimized closely to the theoretical capacity of  $\sim 370 \text{ mA h g}^{-1}$  and safety issues related to Lithium deposition are problem [3, 4]. Therefore, the development of the high energy anode materials is essential to achieve high energy densities in LIBs for EV and ESS applications.

As shown in Figure 1.2, silicon is considered as one of the most promising anode material for LIBs, owing to its high theoretical capacity ( $4200 \text{ mA h g}^{-1}$ ), nontoxic, low cost and abundance. However, the huge volume change ( $>300\%$ ) during the lithium insertion/extraction process leads to poor cycling and rate performances, which severely limits its applications. This volume change causes severe pulverization and polarization of Si electrode

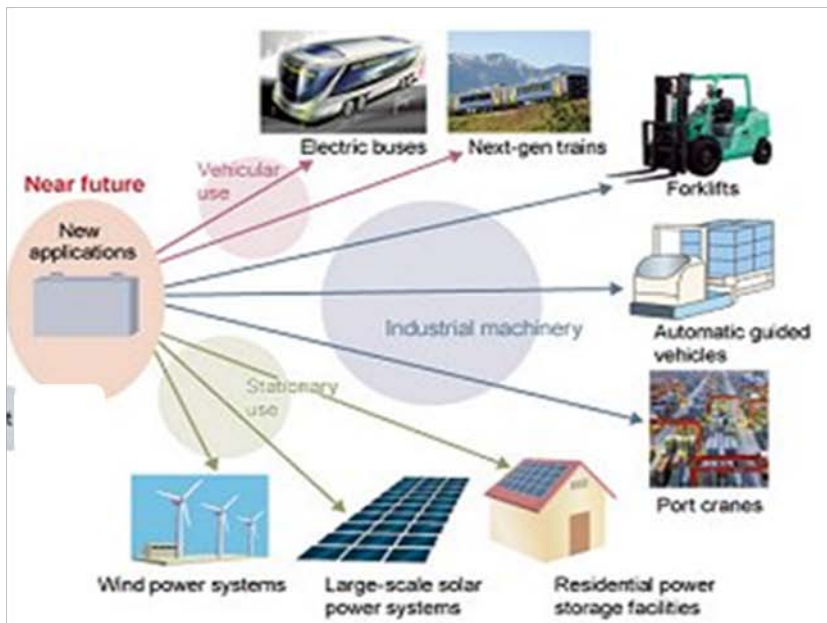
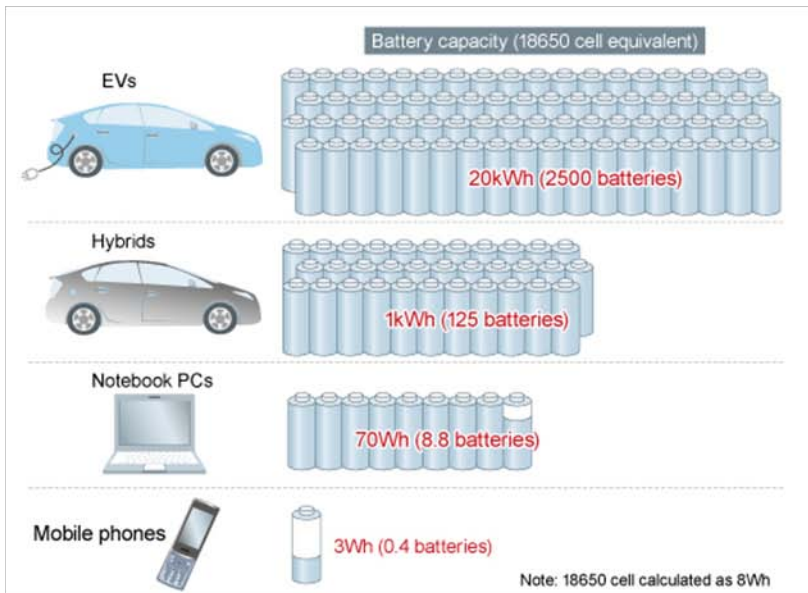


**Figure 1.1** The increasing demand for high energy and power density due to Electric vehicle and Energy storage system. Adapted from Ref [35] (Nikkei Electronics Asia, 2010, February)

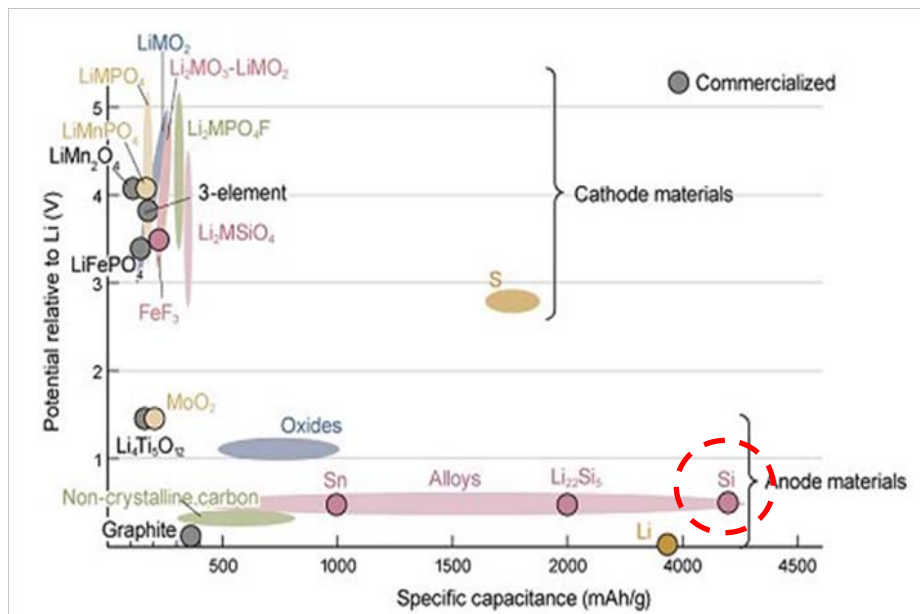


**Figure 1.2** Schematic illustration of materials for cathode and anode materials in terms of capacity and potential currently used or projected for the next generation of LIBs. Adapted from Ref [35] (Nikkei Electronics Asia, 2010, February)

and continuously consumes the limited  $\text{Li}^+$  source from electrolyte to form solid-electrolyte interphase (SEI) [5, 6] as shown in Figure 1.3.

There are numerous approaches in improving the cyclability and the conductivity of Si-based anode materials, such as modification of morphologies to nanospheres [7], nanotubes [8-10], nanowires [11, 12], Si/C composites [13-14], and porous structure [15-16].

Recently, many researchers have synthesized such porous structure which shows better capability to withstand stresses arising from the volume changes than those of the bulk materials. For example, Cui's group has proposed a hierarchical structured silicon anode which is inspired by the structure of pomegranate [15]. The hierarchical arrangement which has void spaces in between particles can make a stable SEI and alleviate the volume stress during alloying-dealloying. Hyeon's group has also proposed self- assembled  $\text{Fe}_3\text{O}_4$  nanoparticle clusters as high performance anode [16]. These approaches have exhibited excellent cyclic stability and rate ability due to their elaborate design. However, these bottom-up assembly usually quires a toxic precursor such as  $\text{SiH}_4$  or  $\text{SiCl}_4$  and high-cost complex process. So there are still some limitations for large-scale synthesis.

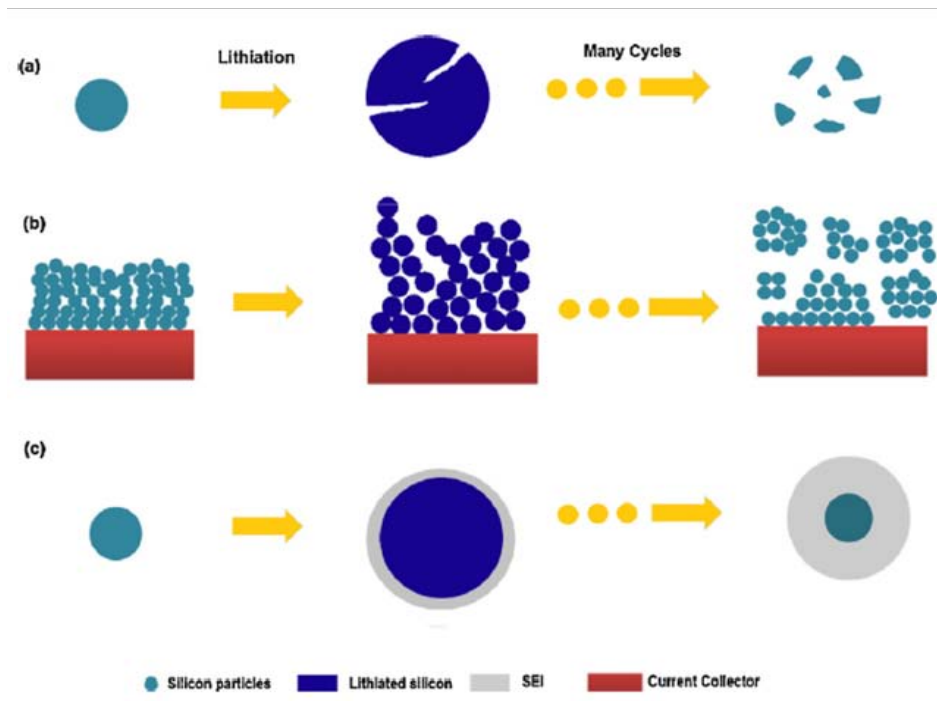


**Figure 1.3** Silicon electrode failure mechanisms : (a) material pulverization. (b) Morphology and volume change of the silicon electrode. (c) Continuous SEI growth during cycle. Adapted from Ref [6] (H. Wu and Y. Cui, Nano Today, 2012, 7, 414.)

On the other hand, the top-down approach is more attractive compared to bottom-up approach due to its low-cost and scalability of the synthesis. For example, Cho's groups made porous bulk Si particles by thermal annealing and etching of physical composites by combining butyl-capped Si gel and SiO<sub>2</sub> [17]. Their material showed the excellent rate capability and stable cycle performance due to the pores acts that act as buffer layer against severe volume changes. Park et al. report a simple route to produce micro-porous bulk Si materials by combining electroless metal deposition with metal assisted chemical etching process [18]. Ran Yi et al. have developed a facile route to produce interconnected micro sized porous Si using the disproportionation of SiO by heating [19]. However, these reports still have some barriers like cost and scalability issues. In contrast, magnesiothermic reduction can produce porous silicon structure from silica at relatively low temperature, and has the advantages of being a low cost and environmentally friendly process. Additionally, the structure and the shape of the precursor can be preserved after this process [20-25]. Recently, there have been increasing number of reports using magnesiothermic reduction to produce macro porous structure [20], nanosheet [21], nanowire [22], nanotube [23], hollow spheres [24], yolk-shell [25] as shown in Figure 2.4.

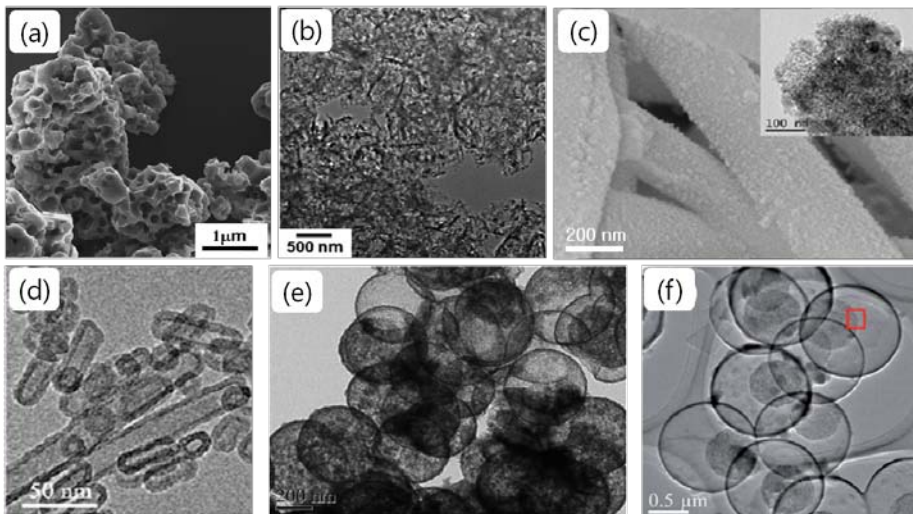
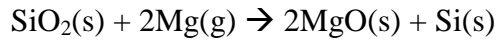
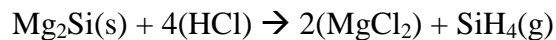


**Figure 1.4** Various porous silicon structure by magnesiothermic reduction : (a) macro porous [20] (b) nanosheet [21] (c) nanowire [22] (d) nanotube [23] (e) hollow sphere [24] (f) yolk-shell [25].

As an example, Sandhage group reported the synthesis of porous Si from SiO<sub>2</sub> by the shape-preserving magnesiothermic reduction [26]. The reduction of SiO<sub>2</sub> by magnesium progresses as shown below:



The resulting material is then immersed with dilute HCl to remove MgO and Mg<sub>2</sub>Si in the core of the sphere. The sites of MgO and Mg<sub>2</sub>Si are converted to porous space. However the mechanism of magnesiothermic reduction is not fully established. For example, Barati et al suggested the Mg<sub>2</sub>Si, intermetallic compound, might be involved during the early stages of reduction process and then after awhile Mg<sub>2</sub>Si is consumed in the SiO<sub>2</sub> reduction [36]. If Mg<sub>2</sub>Si is not sufficiently converted to Si, it could be a main reason for significant gas generation and disintegration of the sample during etching as shown in the reaction written below:



In order to avoid these problems, the reaction conditions, such as Mg vapor pressure, reaction time, molar ratio, temperature, are important and require delicate control.

Another limitation of silicon is its low electrical conductivity. Surface coating with carbon, metal oxides, and conducting polymer are few one of the options to improve conductivity [27-31] (Table 1). The choice of coating materials should be based on high conductivity, mechanical strength and chemical stability. Although the carbon materials have been mainly used as coating materials, the carbon coating would be destroyed easily after repeated large volume changes during cycles. Moreover, the new surface of silicon would be exposed to electrolyte and an additional reduction of electrolyte would take place and cover the new surface of silicon.

Convertible oxides are considered as candidates for coating materials [32]. Among them, titanium silicide ( $\text{TiSi}_2$ ) is highly electrically conductive (resistivity  $\sim 10 \mu\Omega$ ), thermally stable, mechanical robust, and light-weight [33].  $\text{TiSi}_2$  also does not react with lithium [32]. Park et al. reported a simple route for combining titanium silicide and silicon via the silicothermic reduction. It exhibits a highly stable solid electrolyte interface during cycling and good rate ability [34].

Material	$\rho$ ( $\Omega \cdot \text{m}$ ) at 20 °C	$\sigma$ (S/m) at 20 °C	Reference
Aluminium	$2.82 \times 10^{-8}$	$3.5 \times 10^7$	[27]
Carbon (amorphous)	$5 \times 10^{-4}$ to $8 \times 10^{-4}$	$1.25 \times 10^3$ to $2 \times 10^3$	[27]
Carbon (graphene)	$1 \times 10^{-8}$	-	[28]
Carbon (graphite)	$2.5 \times 10^{-6}$ to $5.0 \times 10^{-6}$ // basal plane	$2 \times 10^5$ to $3 \times 10^5$ // basal plane	[31]
	$3.0 \times 10^{-3} \perp$ basal plane	$3.3 \times 10^2 \perp$ basal plane	
Copper	$1.68 \times 10^{-8}$	$5.96 \times 10^7$	[29]
Gold	$2.44 \times 10^{-8}$	$4.10 \times 10^7$	[27]
Iron	$1.0 \times 10^{-7}$	$1.00 \times 10^7$	[27]
Lead	$2.2 \times 10^{-7}$	$4.55 \times 10^6$	[27]
Manganese	$4.82 \times 10^{-7}$	$2.07 \times 10^6$	[30]
Nickel	$6.99 \times 10^{-8}$	$1.43 \times 10^7$	
PEDOT:PSS	$1 \times 10^{-3}$ to $1 \times 10^{-1}$	$1 \times 10^4$ to $1 \times 10^3$	
Platinum	$1.06 \times 10^{-7}$	$9.43 \times 10^6$	[27]
Silicon	$6.40 \times 10^2$	$1.56 \times 10^{-3}$	[27]
Silver	$1.59 \times 10^{-8}$	$6.30 \times 10^7$	[27]
Tin	$1.09 \times 10^{-7}$	$9.17 \times 10^6$	
Titanium	$4.20 \times 10^{-7}$	$2.38 \times 10^6$	

**Table 1** this table shows the resistivity and conductivity of various materials at 20°C

Herein we present a facile way for synthesizing high performance porous silicon@titanium silicide (P-Si@TiSi<sub>2</sub>) sphere anode material using the magnesiothermic reduction process for SiO<sub>2</sub>@TiO<sub>2</sub> composite. During the reduction reaction, the TiO<sub>2</sub> layer was firstly reduced to Ti and then SiO<sub>2</sub> layer was reduced to Si. In addition, Ti and Si produced TiSi<sub>2</sub> layer at high temperature [37]. Taking advantages of the porous structure and high electrically conductive coating layer allow this anode material to exhibit a significantly enhanced electrochemical performance.

## **Chapter 2. Experimental**

### **2.1 Preparation of material**

#### **Preparation of SiO<sub>2</sub> nanoparticle (600~700 nm)**

Stöber method was used to preparing SiO<sub>2</sub> nanoparticle. 200 ml of absolute ethanol, 20 g of DI water, and 12 g of ammonium hydroxide solution (28~30 %) were mixed and magnetically stirred for 30 minutes. Then, 12 g of tetraethylorthosilicate was added to the solution. After 6 hr, SiO<sub>2</sub> nanoparticle was collected by centrifugation and washed with ethanol for 3 times. Collected SiO<sub>2</sub> nanoparticle was dried under vacuum at 80 °C.

#### **Preparation of SiO<sub>2</sub>@TiO<sub>2</sub> nanoparticle**

500 mg of SiO<sub>2</sub> nanoparticle was distributed in 500 ml of cosolvent composed of ethanol and acetonitrile (v/v=1:1). 2.5 ml of ammonium hydroxide solution (28~30%) was added to the solution, and then stirred for 30 minutes. To the mixture solution, titanium butoxide solution, containing 0.5 ml of titanium butoxide, 10 ml of ethanol, and 10 ml of acetonitrile, was injected and allowed to react

for 2 hr. Product was collected by centrifugation and washed with ethanol for 3 times. Collected product was dried under vacuum at 80 °C. The coating thickness of TiO<sub>2</sub> can be modified through controlling the reaction time and titanium butoxide concentration.

### **Preparation of P-Si@TiSi<sub>2</sub> nanoparticle**

The as-synthesized SiO<sub>2</sub>@TiO<sub>2</sub> nanoparticle and magnesium powder put in the steel boat according to the molar ratio of SiO<sub>2</sub>@TiO<sub>2</sub> to Mg = 1 : 2.5. Such steel boat was put into the cylindrical sealing reactor and assembled in argon filled glovebox. The assembled cylindrical sealing reactor was heated in a tube furnace at 700 °C for 6h under argon. The samples were immersed in 1M HCl for 8hr to selectively remove MgO and Mg<sub>2</sub>Si. And then the samples were washed by DI water for three times and vacuum drying.

### **Preparation of P-Si nanoparticle**

For comparison, we have synthesized the P-Si spheres (~600nm) which were synthesized by direct magnesiothermic reduction of SiO<sub>2</sub> spheres. According to the same synthesis procedure for P-Si@TiSi<sub>2</sub> spheres.

## **2.2 Preparation of composite electrode**

The working electrode was prepared by mixing active material (70 wt. %), super P (as a conductive agent) (15 wt. %) and polyamideimide (PAI) binder (15. %). The slurry was uniformly spread onto a copper foil through a doctor blade method and dried in a vacuum oven at 60°C for 1hour. To activate the PAI binder, the as-prepared electrode was heated at 350°C for 90min under argon atmosphere and dried again in a vacuum over at 120°C for 8 hour.

## **2.3 Preparation of half cell**

2016-type coin cell were assembled with the as-prepared electrode, a polypropylene separator, lithium foil as the counter electrode and 1.5 M LiPF<sub>6</sub> solution in a 5 : 25 : 70 (v/v) mixture of EC, FEC, DEC. The assembly was performed in an argon atmosphere glove box.

## **2.4 Characterization**

**Scanning electron microscopy (SEM), energy dispersive X-ray spectroscopy (EDS)**

The morphologies of samples were carried out using a field

emission electron microscope (FE-SEM, AURIGA, Carl Zeiss). SEM samples were prepared drop-blowing the powder samples onto carbon tape.

### **X-ray diffraction (XRD)**

X-ray diffraction patterns were recorded using High Power XRD from Rigaku Corp. with Cu K $\alpha$  radiation (Model : D-MAX2500-PC). The diffraction data is collected in the  $2\theta$  range of  $20^\circ \sim 80^\circ$  with a step of  $4^\circ/\text{min}$ .

### **High resolution transmission electron microscopy (HR-TEM), energy dispersive X-ray spectroscopy (EDS)**

In order to confirm the presence of porous structure, coating layer and compositions, TEM and EDS analysis were carried out on a JEOL JEM-2100F electron microscope. The samples were prepared by drop-drying from their diluted aqueous suspensions onto the carbon grid.

### **Brunaur-Emmett-Teller (BET)**

The surface area and pore size distributions of samples were carried from the N<sub>2</sub> adsorption/desorption isotherms recorded at 77K.

Before measurements, the samples were degassed at 150°C for 4hr.

## **2.5 Electrochemical measurement**

Electrochemical measurements were carried out using 2016-type coin cell. The galvanostatic charge-discharge experiment was performed in the potential range 0.01V ~ 1.5V vs. Li/Li<sup>+</sup> with a WBCS3000 cycler (WonA Tech, Korea) at room temperature. Cyclic voltammetry (CV) was carried out from 1.5V to 0.01V vs. Li/ Li<sup>+</sup> at a scan rate of 0.1mV/s using a WBCS3000 cycler (WonA Tech, Korea). Electrochemical Impedance Spectroscopy (EIS) was conducted in the frequency range from 100 kHz to 50 mHz with an AC signal amplitude of 10 mV (Zahner, Germany). The specific capacity and current density were considered on the composite material. In order to check the electrode after cycling, the cycled cell was carefully disassembled and washed by PC in an argon atmosphere glove box and dried.

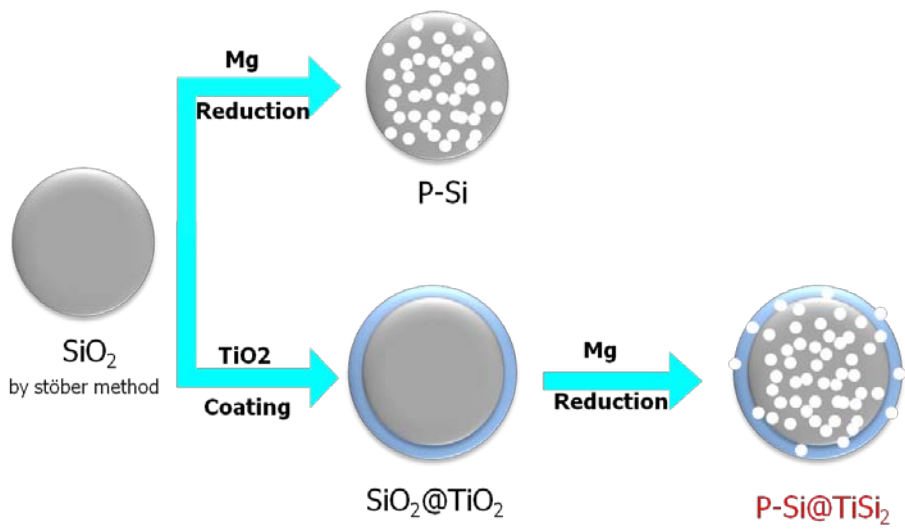
## Chapter 3. Results and discussion

### 3.1 The analysis of powder

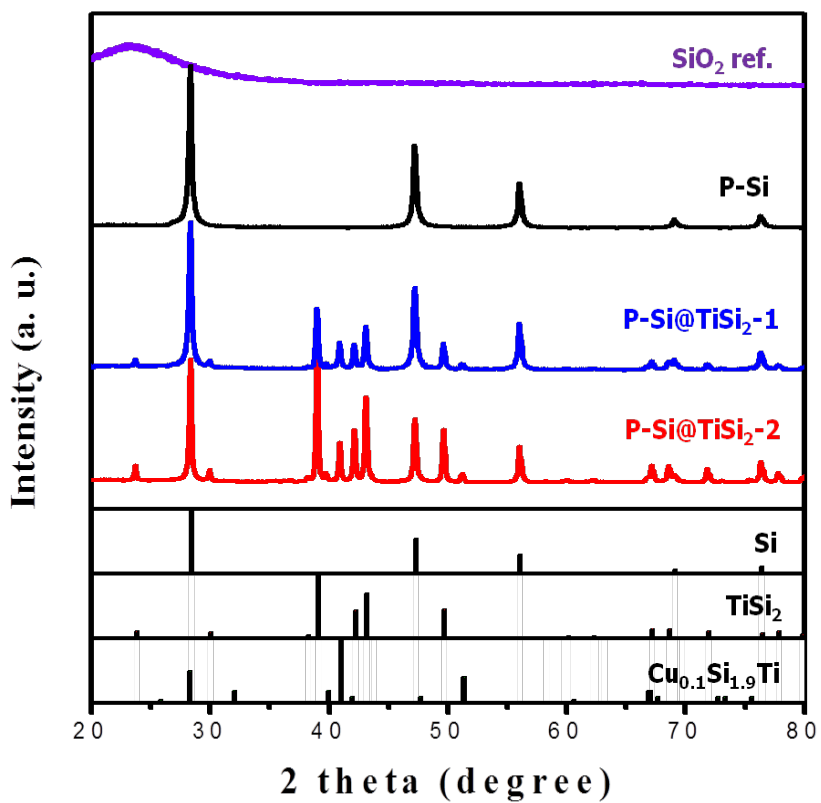
The structure of P-Si@TiSi<sub>2</sub> and P-Si were prepared by magnesiothermic reduction of SiO<sub>2</sub>@TiO<sub>2</sub> composite as shown in Figure 3.1. In brief, SiO<sub>2</sub> spheres were synthesized by stöber method and TiO<sub>2</sub> is uniformly coated onto the surface of SiO<sub>2</sub> spheres via room temperature solution coating method. The coating thickness of TiO<sub>2</sub> can be modified through controlling the reaction time and titanium butoxide concentration. The SiO<sub>2</sub>@TiO<sub>2</sub> powder is enclosed in a steel boat with Mg according to the molar ratio of SiO<sub>2</sub>@TiO<sub>2</sub> to Mg = 1 : 2.5 to conduct magnesiothermic reduction. After etching the reduced powder with dilute HCl to remove MgO and Mg<sub>2</sub>Si, the P-Si@TiSi<sub>2</sub> spheres are finally obtained.

Figure 3.2 shows the X-ray diffraction (XRD) patterns of all the samples. As expected, SiO<sub>2</sub> and SiO<sub>2</sub>@TiO<sub>2</sub> samples exhibit a single broad peak centered at near 23° and 24° indicating the materials are amorphous structure before magnesiothermic reduction. After magnesiothermic reduction and HCl etching, all the samples exhibit the sharp diffraction peaks which can be indexed to a diamond structured Si (JCPDS, no. 27-1402). Additional peaks that arise from

TiO<sub>2</sub> coating samples can be indexed TiSi<sub>2</sub> (JCPDS, no. 35-0785) and the weak intensity of Cu<sub>0.1</sub>Si<sub>1.9</sub>Ti (JCPDS, no. 23-0964) as impurities. This Cu element came from Cu gasket which is used to seal the reactor for magnesiothermic reduction. As the amount of TiO<sub>2</sub> is increased, the peaks intensity of the TiSi<sub>2</sub> is increased accompanied by abatement of the Si peaks.



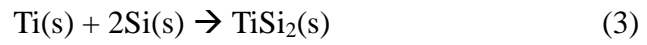
**Figure 3.1** Schematic structure illustration of the synthesis of P-Si and P-Si@TiSi<sub>2</sub> sphere.



**Figure 3.2** XRD patterns of SiO<sub>2</sub>, P-Si, P-Si@TiSi<sub>2</sub>-1 and P-Si@TiSi<sub>2</sub>-2 spheres.

The field emission scanning electron microscopy (FE-SEM) images (Figure 3.3) show spherical particles with diameters of 500nm – 600nm and the particles' morphologies are uneven. All the three samples maintain their structure well after reduction. However, some of P-Si particles are clearly broken (Figure 3.3a). On the other hand, the P-Si@TiSi<sub>2</sub> particles are maintaining their structure relatively well due to the TiSi<sub>2</sub> coating layer which is helpful in maintaining its original structure. Additionally, the uneven morphology of P-Si@TiSi<sub>2</sub>-1 and P-Si@TiSi<sub>2</sub>-2 (Figure 3.3c, 3.3e) are also shown. The TiO<sub>2</sub> layer also has become porous structure of TiSi<sub>2</sub> due to conversion reaction with Mg (Figure 3.3d, 3.3f). The morphology of P-Si@TiSi<sub>2</sub>-1 and P-Si@TiSi<sub>2</sub>-2 is much uneven than that of P-Si due to TiSi<sub>2</sub>. Figure 3.3e shows the excess TiO<sub>2</sub> coating layer, which could be a cause of aggregation of particles.

The formation of TiSi<sub>2</sub> can be explained as shown in following reactions : (1) In accordance with the Ellingham diagram, the TiO<sub>2</sub> was reduced to Ti firstly by the magnesiothermic reduction [39]. (2) Subsequently SiO<sub>2</sub> was also reduced to Si by the magnesiothermic reduction. (3) The reduced Ti and Si are combined to form TiSi<sub>2</sub> at high temperature condition [40]. The reactions are as shown below:



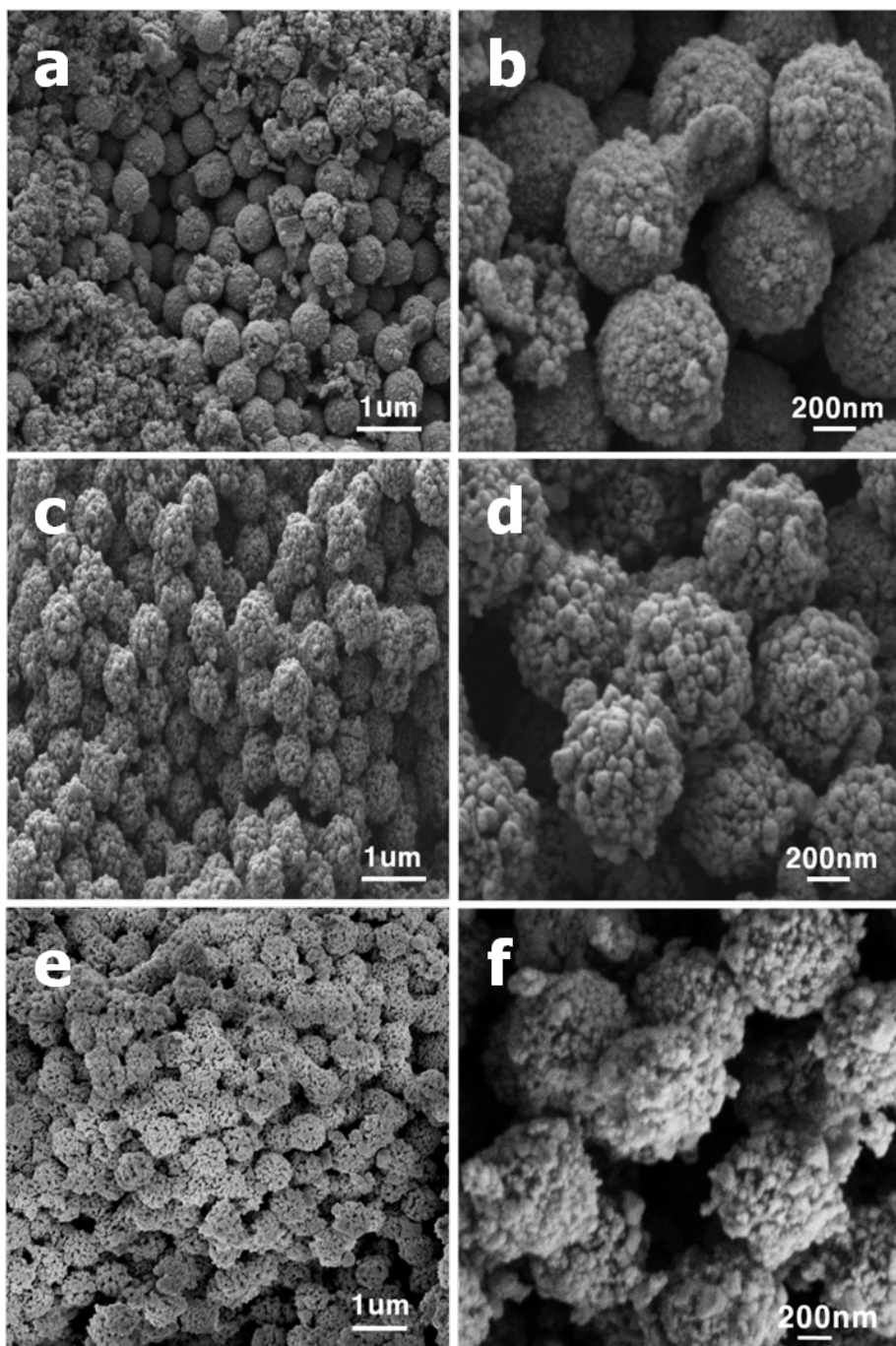
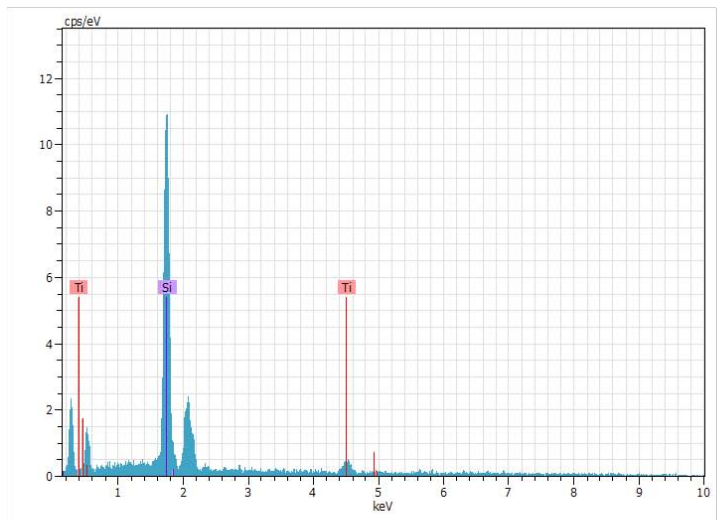
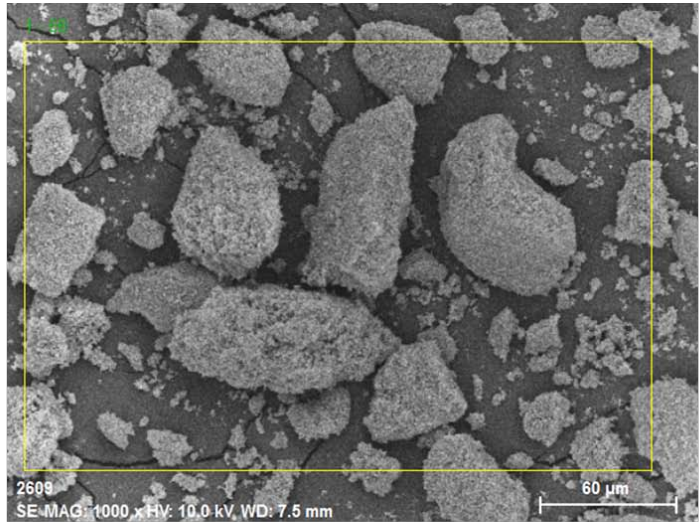


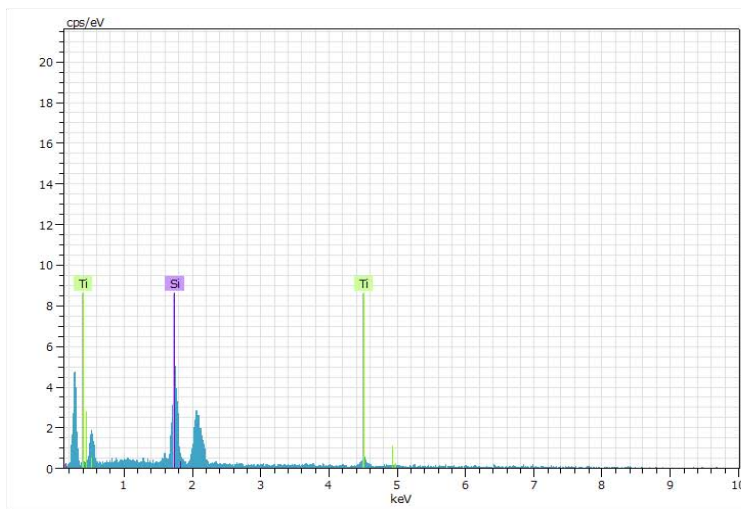
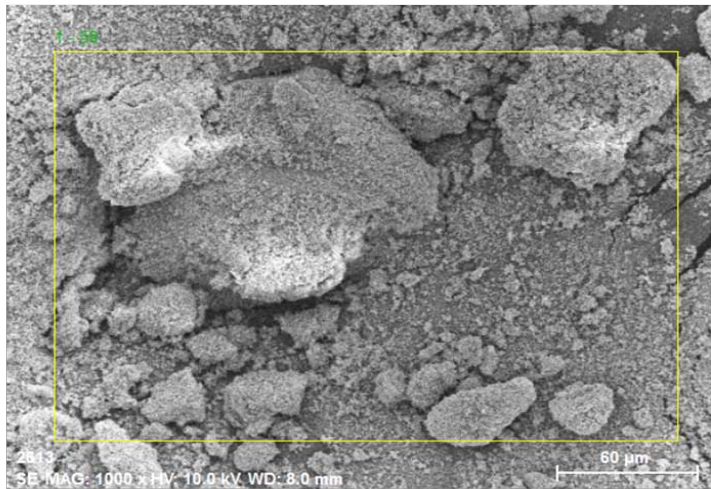
**Figure 3.3** SEM images of P-Si (a, b), P-Si@TiSi<sub>2</sub>-1 (c, d), P-Si@TiSi<sub>2</sub>-2 (e, f).

The EDS elemental mapping of the  $\text{TiSi}_2$  composite (Figure 3.4, 3.5) was carried out to identify the ratio of Si and Ti. If oxygen is not considered due to its uncertain value, the P-Si@ $\text{TiSi}_2$ -1 and P-Si@ $\text{TiSi}_2$ -2 are composed of Si (87 wt. %), Ti (12.9 wt. %) and Si (76.6 wt. %), Ti (23.4 wt. %) respectively. If we make an assumption that all Ti is changed to  $\text{TiSi}_2$  and there are no other elements. The weight of Si contained in P-Si@ $\text{TiSi}_2$ -1 and P-Si@ $\text{TiSi}_2$ -2 are 71.7 wt. % and 48.7 wt. % respectively. Since Si is the only active material that generates capacity, the specific capacity can be calculated as 2566  $\text{mAh g}^{-1}$  and 1743  $\text{mAh g}^{-1}$  for P-Si@ $\text{TiSi}_2$ -1 and P-Si@ $\text{TiSi}_2$ -2 by considering that the specific capacity of Si at room temperature is about 3580  $\text{mAh g}^{-1}$ . These values are roughly matched with the specific capacity of P-Si@ $\text{TiSi}_2$ -1 and P-Si@ $\text{TiSi}_2$ -2 composites (Figure 3.10).



Element	Series	unn. [wt.%]	C norm. [wt.%]	C Atom. [at.%]	Error (1 Sigma) [wt.%]
Silicon	K-series	29.99	87.10	92.01	1.32
Titanium	K-series	4.44	12.90	7.99	0.31
Total:		34.43	100.00	100.00	

**Figure 3.4** EDS mapping of P-Si@TiSi<sub>2</sub>-1



Element	Series	unn. [wt.%]	C norm. [wt.%]	C Atom. [at.%]	Error (1 Sigma) [wt.%]
Silicon K-series		14.55	76.62	84.82	0.70
Titanium K-series		4.44	23.38	15.18	0.32
Total:		19.00	100.00	100.00	

**Figure 3.5** EDS mapping of P-Si@TiSi<sub>2</sub>-2

Further detail information into the particle structure is obtained by a high resolution transmission electron microscope (HR-TEM) images at different magnifications, which demonstrate that all of the particles have porous structure (Figure 3.6 a-f). First of all, Figure 3.6 presents that the P-Si has the distinct lattice fringes spaced 0.31 nm, which correspond with interplanar spacing of Si (111), which is confirmed by the fast fourier transform (FFT) pattern. Moreover, it seems that the grain size is getting bigger and  $\text{TiSi}_2$  is aggregated on the outside of spheres as the amount of  $\text{TiO}_2$  coating layer increases. The amorphous  $\text{TiO}_2$  layers are coated uniformly on the surface of the  $\text{SiO}_2$  particles with an average thickness of ~10 nm and 25 nm for P-Si@ $\text{TiSi}_2$ -1 and P-Si@ $\text{TiSi}_2$ -2 respectively (Figure 3.7a, b). The  $\text{TiSi}_2$  distributed outside of the sphere is confirmed by the fast fourier transform (FFT) pattern (Figure 3.7c, d) and the intensity line scans of the particle cross section (Figure 3.8a, b).

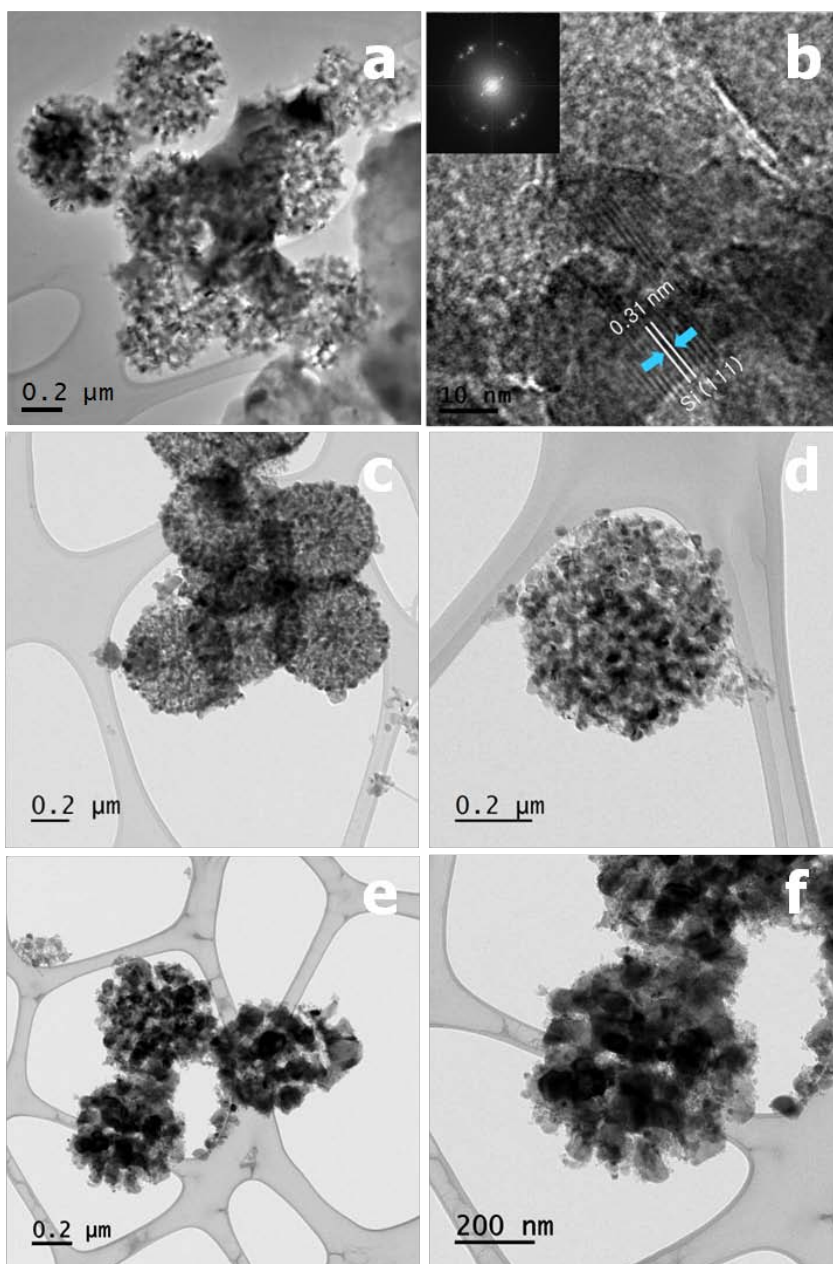


**Figure 3.6** TEM images of P-Si (a, b), P-Si@TiSi<sub>2</sub>-1 (c, d), P-Si@TiSi<sub>2</sub>-2 (e, f).

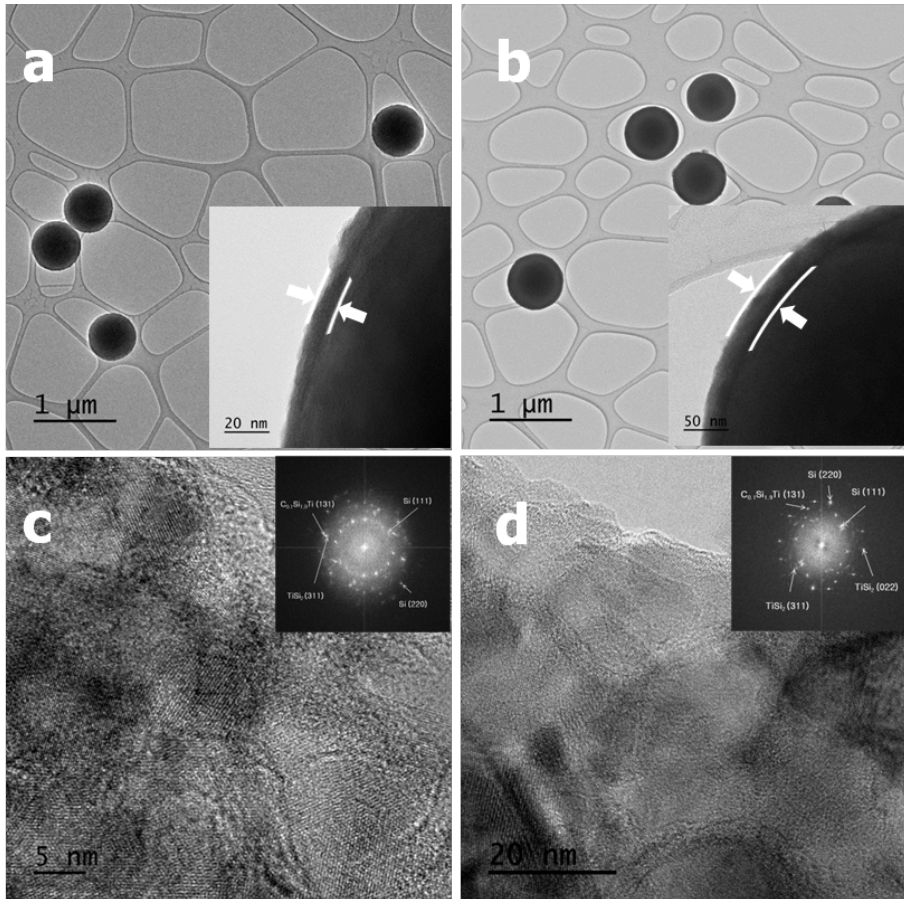


**Figure 3.7** TEM images of P-Si@TiSi<sub>2</sub>-1 (a), P-Si@TiSi<sub>2</sub>-2 (b) before magnesian reduction. TEM image of P-Si@TiSi<sub>2</sub>-1 (c), P-Si@TiSi<sub>2</sub>-2 (f) after magnesian reduction.

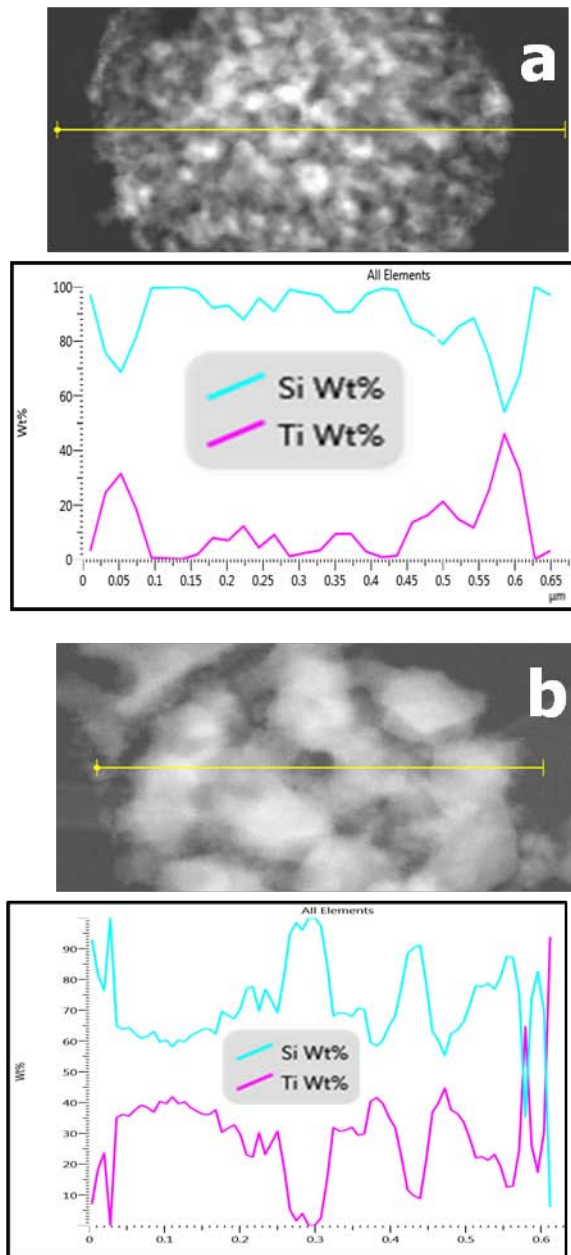


**Figure 3.8** EDS line scan data of P-Si@TiSi<sub>2</sub>-1 (a), P-Si@TiSi<sub>2</sub>-2 (b)

The specific surface area and the pore size distribution of porous structure particles were investigated by the nitrogen adsorption and desorption measurement. All the samples exhibit an isotherm curve with a hysteresis loop at the high pressure region (Figure 3.9a), which indicates a characteristic of different processes while measuring adsorption and desorption of mesopores and macropores. According to the results of the nitrogen adsorption and desorption, the P-Si exhibit a BET surface area  $154.8 \text{ m}^2 \text{ g}^{-1}$ , which is much higher than those of the other composites. The P-Si@TiSi<sub>2</sub>-1 exhibits a BET surface area of  $61.4 \text{ m}^2 \text{ g}^{-1}$ , higher than that of the P-Si@TiSi<sub>2</sub>-2 ( $34.7 \text{ m}^2 \text{ g}^{-1}$ ), suggesting the TiSi<sub>2</sub> modification contributes to the reduction of the surface area. The reaction between Si and Ti leads to a decrease in surface area.

The corresponding pore size distribution curves are plotted from the Barrett-Joyner-Halenda (BJH) method (Figure 3.9b). The P-Si exhibit an average pore size around 25 nm. Whereas the P-Si@TiSi<sub>2</sub>-1 exhibit large mesopores around 50 nm and the P-Si@TiSi<sub>2</sub>-2 exhibit macropores around 100 nm. It's because that capillary condensation and saturation pressure occur almost simultaneously, which is a maximum limit of pore size by the gas adsorption technique. The amount of TiSi<sub>2</sub> is inversely proportionate to the pore diameter.

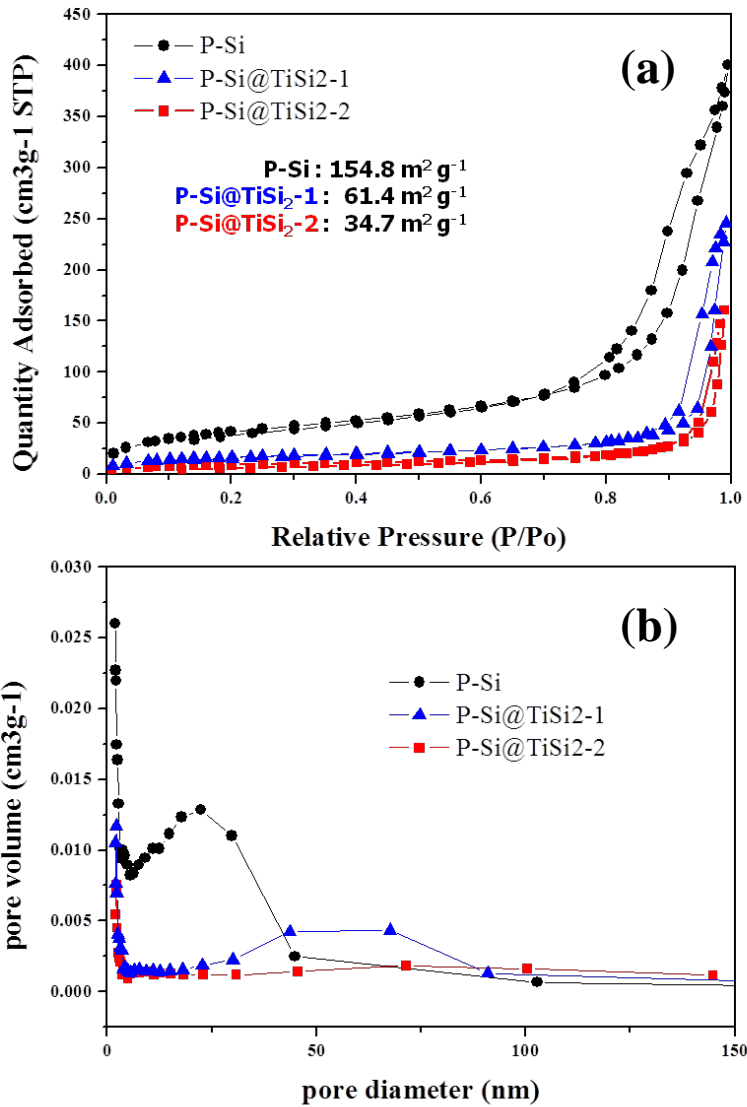


**Figure 3.9** Nitrogen adsorption-desorption isotherms at 77K (a) and pore size distribution (b) of P-Si, P-Si@TiSi<sub>2</sub>-1, P-Si@TiSi<sub>2</sub>-2.

### 3.2 The electrochemical analysis

The electrochemical performance of the porous structure particles as the anode was tested by galvanostatic discharge and charge between 0.01 V and 0.15 V. The first discharge profile exhibits a long and flat plateau below 0.1 V owing to the structure change of crystalline Si to amorphous Si with the formation of  $\text{Li}_x\text{Si}$  [41, 42]. The decomposition of the electrolyte at the electrode surface start to form SEI layer which is ionically conducting and electronically insulating. The SEI layer prevents further side reaction of electrolyte when the potential is below 1.0 V [43, 44]. Figure 3.10 shows the discharge and the charge voltage profiles during cycles at a current density of  $400 \text{ mA g}^{-1}$ .

The discharge specific capacity of P-Si at the first cycle is the highest as  $2830 \text{ mAh g}^{-1}$  in comparison with  $2390 \text{ mAh g}^{-1}$  of P-Si@TiSi<sub>2</sub>-1 and  $1432 \text{ mAh g}^{-1}$  of P-Si@TiSi<sub>2</sub>-2. As expected, the discharge capacity is reduced as the amount of TiSi<sub>2</sub> is increased, which is expected considering it is an inactive material. However, the specific capacity fading of P-Si during the cycling is also the fastest in comparison with those of P-Si@TiSi<sub>2</sub>-1 and P-Si@TiSi<sub>2</sub>-2. The enhanced cyclic stability of TiSi<sub>2</sub> composites may be caused by the TiSi<sub>2</sub> coating layer, which can maintain the structure and restrain the

continuous growth of SEI layer. However, there is fast capacity fading in between 10<sup>th</sup> cycle and 20<sup>th</sup> cycle in the voltage profile of P-Si@TiSi<sub>2</sub>-2 which has a large amount of TiSi<sub>2</sub> as shown in Figure 3.10c. Excess TiSi<sub>2</sub> may be the cause of the fast capacity fading. However, the overpotential of P-Si@TiSi<sub>2</sub>-1 and P-Si@TiSi<sub>2</sub>-2 at 5<sup>th</sup> cycle is reduced in comparison with that of p-Si due to TiSi<sub>2</sub> coating layer.

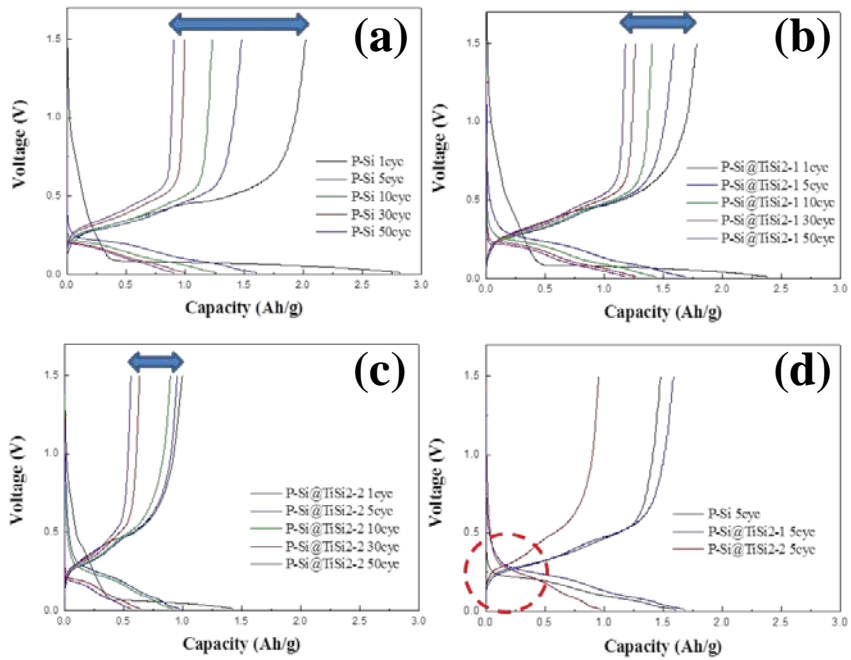


**Figure 3.10** Cycle voltage profile at 1, 5, 10, 30, 50 of (a) P-Si (b) P-Si@TiSi<sub>2</sub>-1 (c) P-Si@TiSi<sub>2</sub>-2 (d) Comparison with three samples at 5cycle.

Figure 3.11 exhibits the cycling performance of three samples at a current density of  $400 \text{ mA g}^{-1}$ . All the three samples exhibit capacity fading during cycling, especially in the beginning, which could be attributed to the continuous SEI growth, electrode pulverization, disconnection of active material during lithiation-delithiation [45, 46]. Even though the P-Si has the highest specific capacity at the first cycle, the capacity retention is the lowest at 45 % after 50 cycles. On the other hand, the P-Si@TiSi<sub>2</sub>-1 exhibits the highest capacity retention percent at 66 % after 50 cycles. However, the P-Si@TiSi<sub>2</sub>-2 has an inflection point between 10<sup>th</sup> cycle and 20<sup>th</sup> cycle and shows 56% retention of the capacity after 50 cycles. The cause could be that the aggregated P-Si@TiSi<sub>2</sub>-2 particles are separated due to the volume change during cycling. On this account, the P-Si@TiSi<sub>2</sub>-2 particles may increase the internal resistance caused by a loss of the contact area between Si and the carbon particle, which is conducting agent. However, the TiSi<sub>2</sub> coated composites exhibit relatively stable cycle retention while the P-Si without TiSi<sub>2</sub> coating layer displays drastically decreased specific capacity in the beginning cycles due to the difficulty of maintaining structure during charging and discharging. Moreover, the rate capability of the three samples are carried out at various rates ( $400 \text{ mA g}^{-1} - 3200 \text{ mA g}^{-1}$ ) between 0.01V and 0.15V as

shown in Figure 3.11b. The P-Si exhibits the capacity retention of 1% at a high rate of  $3200 \text{ mA g}^{-1}$  compared to that of the  $400 \text{ mA g}^{-1}$ . On the other hand, The  $\text{TiSi}_2$ -1 and  $\text{TiSi}_2$ -2 showed significantly enhanced rate capabilities, 28 % and 32% respectively. These results mean the  $\text{TiSi}_2$  coating layers play an important role in showing excellent electrochemical performances. The results indicate that the  $\text{TiSi}_2$  layers on the Si surface can reduce the stress of volume change and maintain high conductivity and form a stable SEI layer.

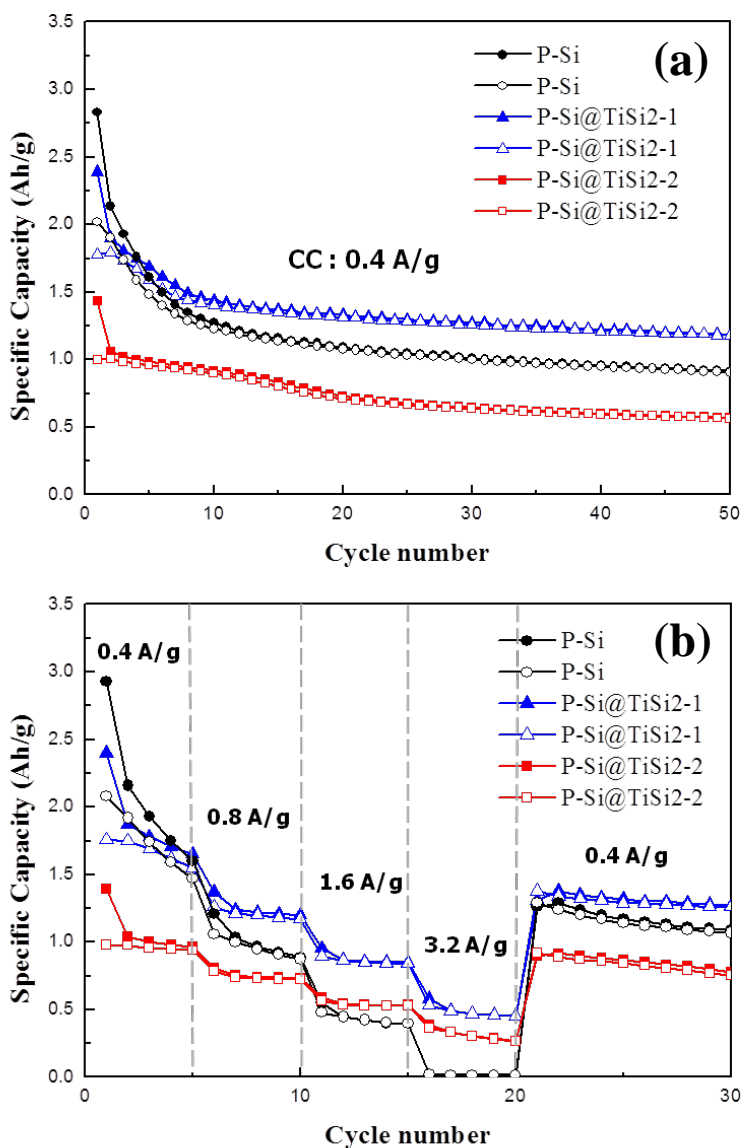
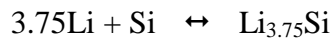


**Figure 3.11** Electrochemical performances of P-Si, P-Si@TiSi<sub>2</sub>-1 and P-Si@TiSi<sub>2</sub>-2. (a) Cycling performance at a current density of 400 mA g<sup>-1</sup> (b) Rate capability at different current densities (400 - 3200 mA g<sup>-1</sup>)

1)

Cyclic voltammetry (CV) was carried out from 1.5 V to 0.01 V vs. Li/ Li<sup>+</sup> at a scan rate of 0.1 mV s<sup>-1</sup> as shown in Figure 3.12. In the first cycle, the peak at 0.8 V in the cathodic process relates with the formation of SEI layer, which disappears in the second cycle [47]. The sharp cathodic peaks at 0.19V are related with the reaction with Si and Li during the lithiation. The two anodic peaks at 0.31V and 0.50V were observed during the delithiation. The reaction is shown below :



The TiSi<sub>2</sub> composites exhibit slightly fast onset potential around 0.4 V at 5th cycle due to the enhance conductivity, which indicates increase of the Li<sup>+</sup> influx (Figure 3.12b).

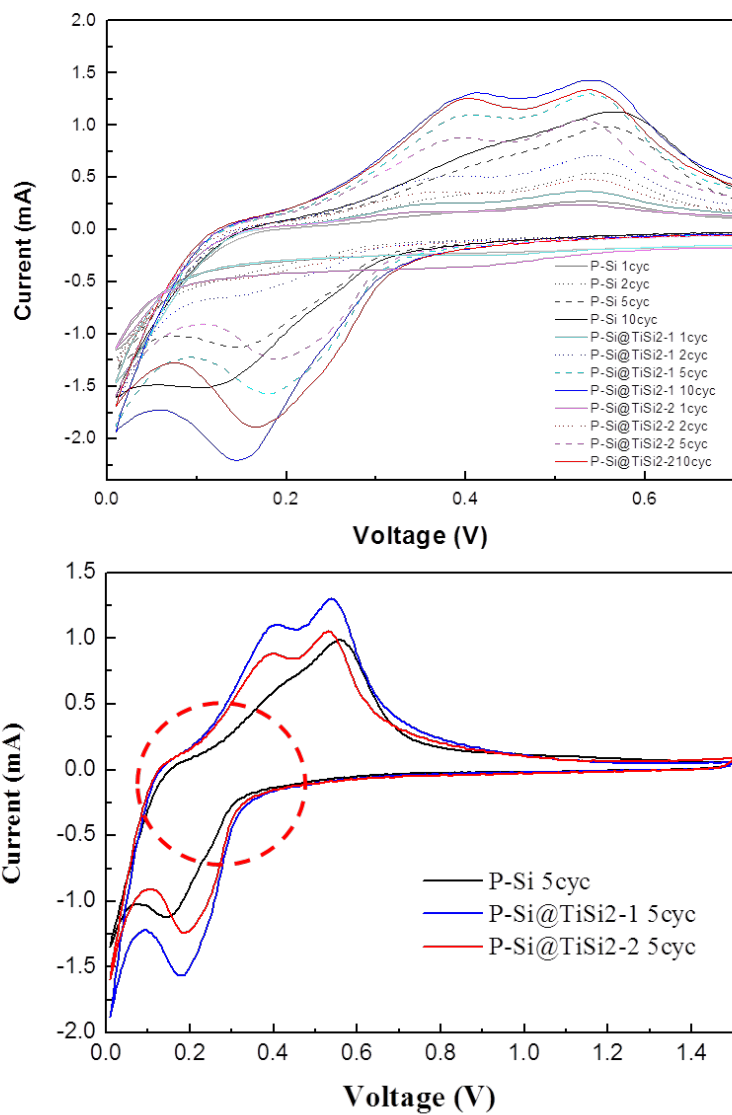


**Figure 3.12** Cyclic voltammetry of P-Si, P-Si@TiSi<sub>2</sub>-1 and P-Si@TiSi<sub>2</sub>-2 from 1.5 V to 0.01 V at a scan rate of 0.1 mV s<sup>-1</sup>. (a) Comparison at 1, 2, 5, 10th cycle. (b) Comparison at 5th cycle.

Moreover, electrochemical impedance spectroscopy (EIS) measurements were carried out to study the resistance of the composites after 3cycles. Figure 3.13 exhibits Nyquist plots of three samples. The  $R_{ct}$  of the P-Si was much higher than those of  $TiSi_2$  composites. This result is corresponds to the cycle and rate performance properties. The  $TiSi_2$  coating layer can enhance conductivity through reducing charge transfer resistance.

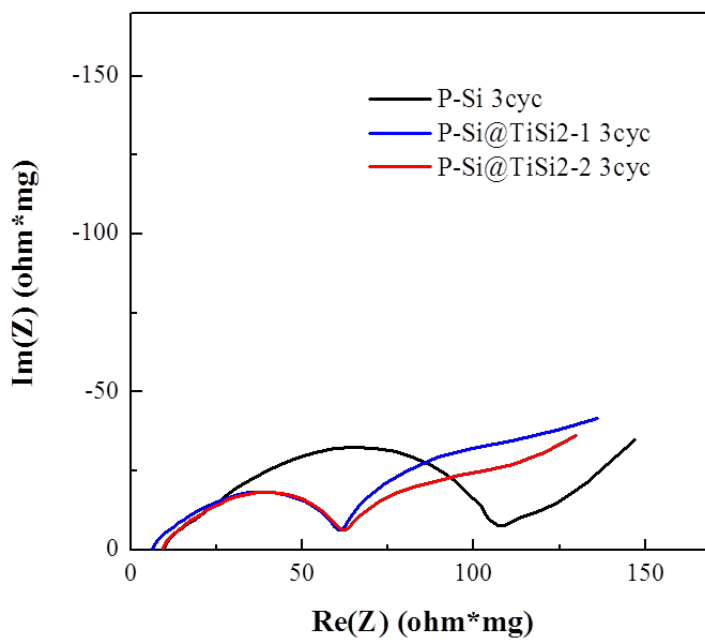


**Figure 3.13** EIS Nyquist plots of the P-Si, P-Si@TiSi<sub>2</sub>-1 and P-Si@TiSi<sub>2</sub>-2 at the lithiated state after 3 cycle.

In addition, the three composites after 50cycles were investigated by SEM as shown in Figure 3.14. The structure of  $\text{TiSi}_2$  composites can be well maintained even after 50cycles while the structure of P-Si was broken. To confirm the structure stability after cycles, we removed the SEI layer using acetonitrile solution [16]. Figure 3.15 shows the structure of  $\text{TiSi}_2$  composites after 50 cycles, and they are similar to that of before cycling by considering that the composite include binder and conducting agent (carbon). The excellent structure stability of the  $\text{TiSi}_2$  composites is reconfirmed.

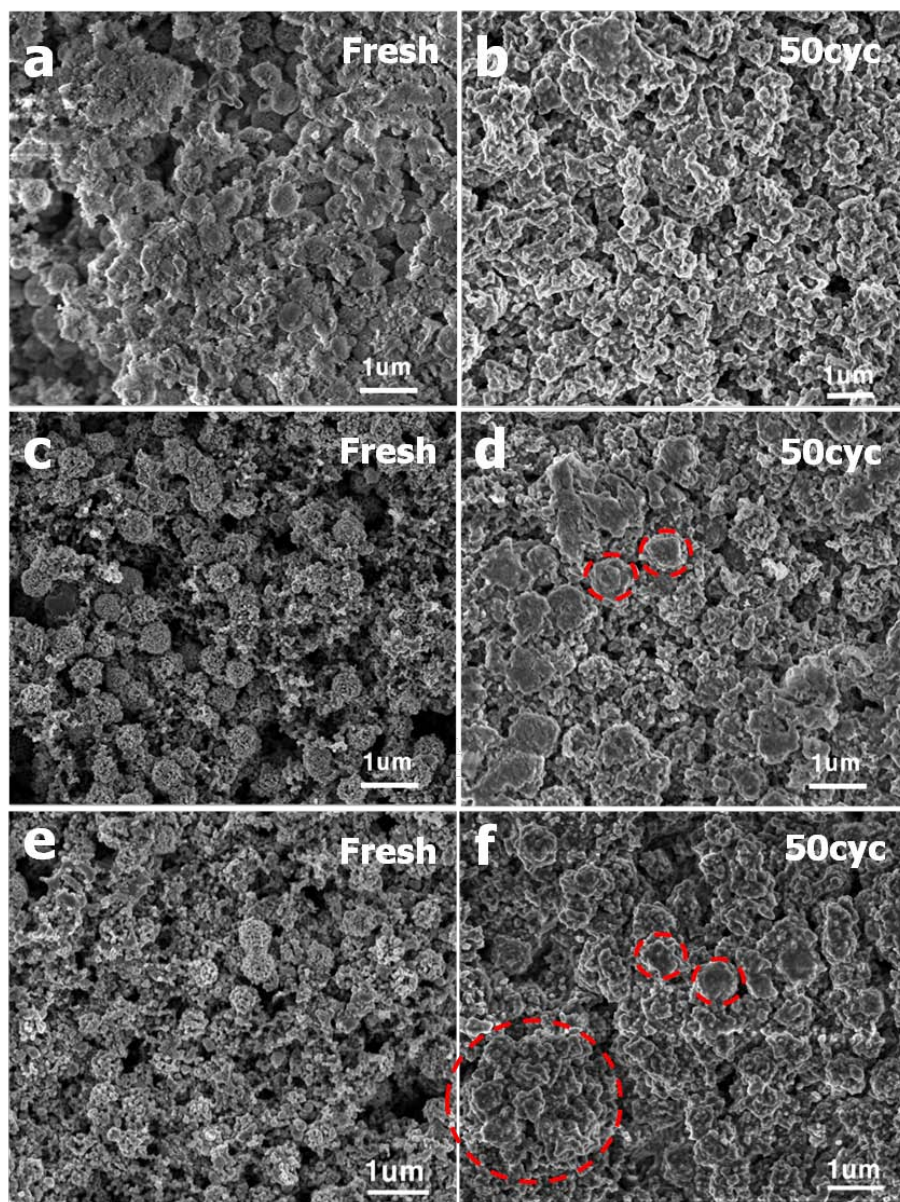


**Figure 3.14** SEM images of P-Si (a, b), P-Si@TiSi<sub>2</sub>-1 (c, d), P-Si@TiSi<sub>2</sub>-2 (e, f) electrodes after 50cycles at 400 mA g<sup>-1</sup>.

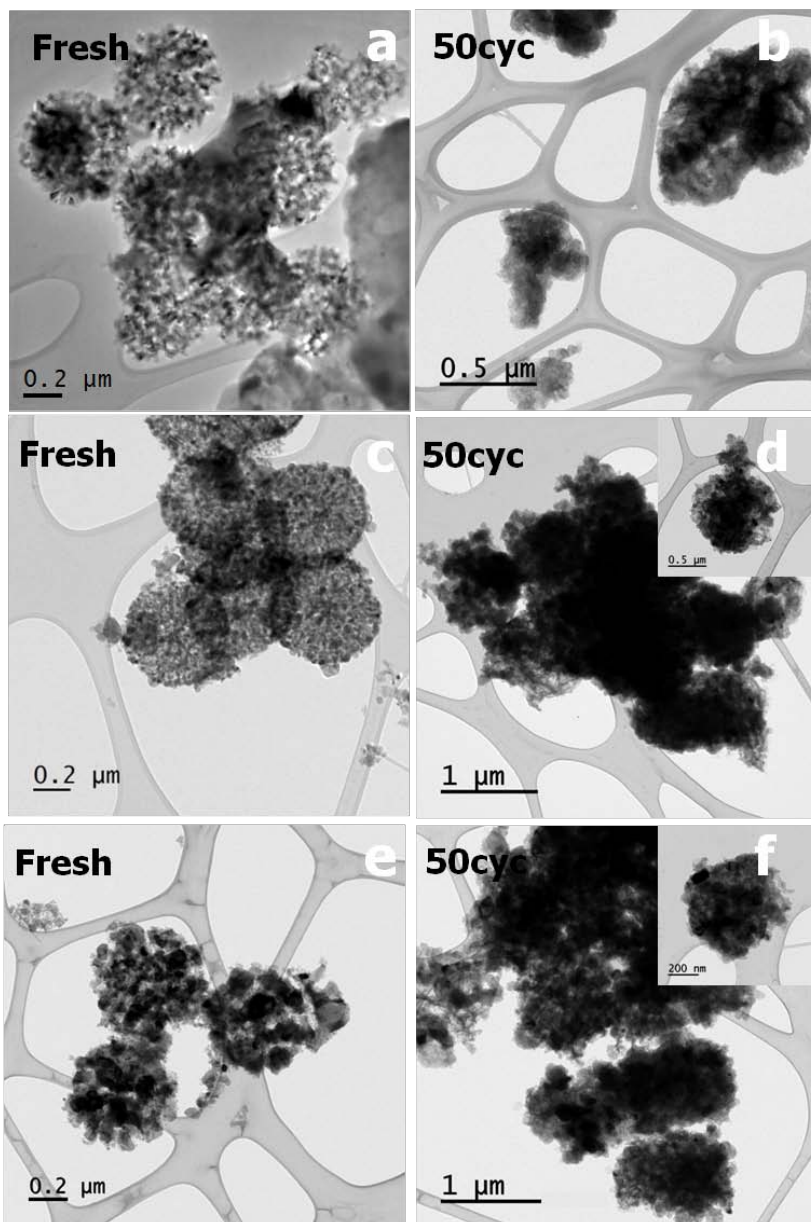


**Figure 3.15** Comparison of three samples before and after cycling. TEM images of P-Si (a), P-Si@TiSi2-1 (c), P-Si@TiSi2-2 before cycling (from powder). TEM images of P-Si (b), P-Si@TiSi2-1 (d), P-Si@TiSi2-2 (f) after 50 cycles (from electrode).

## Chapter 4. Conclusions

In summary, we have developed a facile synthesis method for producing porous Si@TiSi<sub>2</sub> nanospheres from SiO<sub>2</sub>@TiO<sub>2</sub> nanospheres by magnesiothermic reduction. This synthesis is simple and fast process, and applicable in a large scale production at low cost. Taking advantages of the porous structure and high electrically conductive coating layer, this anode material exhibits a significantly enhanced electrochemical performance compared to pure Si. The P-Si@TiSi<sub>2</sub>-1 exhibits a high reversible capacity about 2020 mAh g<sup>-1</sup> at the current density of 400 mA g<sup>-1</sup> and its capacity is about 907 mAh g<sup>-1</sup> even after 50 cycles. Although, the TiSi<sub>2</sub> is inactive toward lithium, which makes it disadvantageous in terms of specific capacity, there are bigger benefits that arise from coating. The TiSi<sub>2</sub> has good electrical conductivity and physical strength, which not only enhances the conductivity but also helps in maintain the composites' structure during cycling. Moreover, the electrochemical performance could be further improved through the size control, composition variation, and structural selectivity. This synthesis is expected to be a new method for producing high capacity anode materials for the next generation LIBs.

## References

- [1] B. Scosati, J. Garche, J. Power Sources, 2010, **195**, 2419.
- [2] A. S. Arico, P. Bruce, B. Scrosati, J. M. tarascon, W. V. Schalkwijk, Nature, 2005, **4**, 366.
- [3] A. K. Shukla, T. P. Kumar, Curr..Sci., 2008, **94**, 314.
- [4] M. Winter, J. O. Besenhard, M. E. Spahr, P. Novak, Adv. Mater., 1998, **10**, 725.
- [5] J. R. Szczech and S. Jin, Energy Environ. Sci., 2011, **4**, 56.
- [6] H. Wu, Y. Cui, Nano Today, 2012, **7**, 414.
- [7] N. Liu, H. Wu, M. T. McDowell, Y. Yao, C. M. Wang, Y. Cui, Nano Lett., 2012, **12**, 3315.
- [8] B. Wang, X. L. Li, X. F. Zhang, B. Luo, M. H. Jin, M. H. Liang, S. A. Dayeh, S. T. Picraux, L. J. Zhi, ACS Nano, 2013, **7**, 1437.
- [9] Y. H. Zhu, W. Liu, X. Y. Zhang, J. C. He, J. T. Chen, Y. P. Wang, T. B. Cao, Langmuir., 2013, **29**, 744.
- [10] Y. Yao, M. T. McDowell, I. Ryu, H. Wu, N. Liu, L. Hu, W. D. Nix, Y. Cui, Nano Lett., 2011, **11**, 2949.
- [11] B. Wang, X. L. Li, X. F. Zhang, B. Luo, Y. B. Zhang, L. J. Zhi, Adv. Mater., 2013, **25**, 3560.

- [12] T. Song, J. Xia, J. H. Lee, D. H. Lee, M. S. Kwon, J. M. Choi, J. Wu, S. K. Doo, H. Chang, W. Park, D. S. Zang, H. Kim, Y. Huang, K. C. Hwang, J. A. Rogers, U. Paik, *Nano Lett.*, 2010, **10**, 1710.
- [13] H. Kim, J. Cho, *Nano Lett.*, 2008, **8**, 3688.
- [14] A. Magasinski, P. Dixon, B. Hertzberg, A. Kvit, J. Ayala and G. Yushin, *Nat. Mater.*, 2010, **9**, 353.
- [15] N. Liu, Z. Lu, J. Zhao, M. T. McDowell, H. W. Lee, W. Zhao, Y. Cui, *Nat. Mater.*, 2014, **3**, 187.
- [16] S. H. Lee, S. H. Yu, J. E. Lee, A. Jin, D. J. Lee, N. Lee, H. Jo, K. Shin, T. Y. Ahn, Y. W. Kim, H. Choe, Y. E. Sung, T. Hyeon, *Nano Lett.*, 2013, **13**, 4249.
- [17] H. Kim, B. H. Lee, J. B. Choo, J. Cho, *Angew. Chem. Int. Ed.*, 2008, **47**, 10151.
- [18] B. M. Bang, J. I. Lee, H. Kim, J. Cho, S. Park, *Adv. Energy Mater.*, 2012, **2**, 878.
- [19] R. Yi, F. Dai, M. L. Gordin, S. Chen, D. Wang, *Adv. Energy Mater.*, 2013, **3**, 295.
- [20] Y. Yu, L. Gu, C. Zhu, S. Tsukimoto, P. A. V. Aken, J. Maier, *Adv. Mater.*, 2010, **22**, 2247.
- [21] W. S. Kim, Y. Hwa, J. H. Shin, M. Yang, H. J. Sohn, S. H. Hong, *Nanoscale*, 2014, **6**, 4297.

- [22] J. K. Yoo, J. Kim, Y. S. Jung, K. Kang, *Adv. Mater.*, 2012, **24**, 5452.
- [23] Z. Wen, G. Lu, S. Mao, H. Kim, S. Cui, K. Yu, X. Huang, P. T. Hurley, O. MaO, J. Chen, *Electrochemistry Commu.*, 2013, **29**, 67.
- [24] M. P. Liu, C. H. Li, H. B. Du, X. Z. You, *Chem. Commun.*, 2012, **48**, 4950.
- [25] Y. Ru, D. G. Evans, H. Zhu, W. Yang, *RSC Adv.*, 2014, **4**, 71.
- [26] Z. Bao, M. R. Weatherspoon, S. Shian, Y. Cai, P. D. Graham, S. M. Allan, G. Ahmad, M. B. Dickerson, B. C. Church, Z. Kang, H. W. Abernathy III, C. J. Summers, M. Liu and K. H. Sandhage, 2007, **446**, 172.
- [27] Raymond A. Serway (1998). *Principles of Physics* (2nd ed.). Fort Worth, Texas; London: Saunders College Pub. p. 602.
- [28] [Newsdesk.umd.edu](http://newsdesk.umd.edu) (2008-03-24). Retrieved on 2014-02-03.
- [29] Douglas Giancoli (2009) [1984]. "25. Electric Currents and Resistance". In Jocelyn Phillips. *Physics for Scientists and Engineers with Modern Physics* (4th ed.). Upper Saddle River, New Jersey: Prentice Hall. p. 658.
- [30] Douglas C. Giancoli (1995). *Physics: Principles with Applications* (4th ed.). London: Prentice Hall.

- [31] Hugh O. Pierson, Handbook of carbon, graphite, diamond, and fullerenes: properties, processing, and applications, p. 61, William Andrew, 1993.
- [32] A. Netz, R. A. Huggins, W. Weppner, Ionics, 2001, **7**, 433.
- [33] J. Chen, J. P. Colinge, D. flandre, R. Gillon, J. P. Raskin, D. Vangoenacker, J. Electrochem Soc., 1997, **144**, 2437.
- [34] O. Park, J. I. Lee, M. J. Chun, J. T. Yeon, S. Yoo, S. Choi, N. S. Choi, S. Park, RSC Advances, 2013, **3**, 2538.
- [35] Nikkei Electronics Asia, 2010, February
- [36] M. Barati , S. Sarder, A. McLean, R. Roy, Journal of Non-Crystalline Solids, 2011, **357**, 18.
- [37] S. Choi, J. C. Lee, O. Park, M. J. Chun, N. S. Choi, S. Park, J. Mater. Chem. A, 2013, **1**, 10617.
- [38] R. Bolivar, B. Friedrich, Synthesis of Titanium via Magnesiothermic Reduction of TiO<sub>2</sub> (Pigment), Proceedings of EMC 2009
- [39] T. B. Reed, Free Energy of Formation of Binary Compounds, MIT press, Cambridge, 1971.
- [40] F. Zhao, X. Cui, B. Wang, J. G. Hou, Appl. Surf. Sci., 2006, **253**, 2785

- [41] H. Jia, P. Gao, J. Yang, J. Wang, Y. Nuli, Z. Yang, *Adv. Energy Mater.*, 2011, **1**, 1036.
- [42] B. M. Bang, H. Kim, H. K. Song, J. Cho, S. Park, *Energy Environ. Sci.*, 2011, **4**, 5013.
- [43] P. Verma, P. Maire, P. Novak, *Electrochim. Acta*, 2010, **55**, 6332.
- [44] R. Ruffo, S.S. Hong, C.K. Chan, R.A. Huggins, Y. Cui, *J. Phys. Chem. C.*, 2009, **113**, 11390.
- [45] C. M. Park, J. H. Kim, H. Kim, H. J. Sohn, *Chem. Soc. Rev.*, 2010, **39**, 3115
- [46] X. L. Wu, Y. G. Guo, L. J. Wan, *Chem.–Asian J.*, 2013, **8**, 1948.
- [47] J. Graetz, C. Ahn, R. Yazami, B. Fultz, *Electrochem.Solid-State Lett.*, 2003, **6**, A19

## 초 록

리튬 이온 전지는 주로 소형 휴대용 장치에 주로 이용되어 왔지만 최근 들어 중대형의 전기 자동차나 에너지 저장 시스템의 시장이 열리면서 고용량 고에너지 밀도에 대한 수요가 크게 증가하고 있다. 이론용량이 가장 크고 값도 싸고 풍부한 실리콘은 차세대 고용량 음극 소재로서 각광 받고 있지만 충/방전시에 수반되는 큰 부피변화와 낮은 전도성 때문에 상용화에 제약을 받고 있다.

본 연구에서는 이를 개선하기 위해 마그네슘 열 환원법을 통해 다공성 구조의 실리콘을 만들고 동시에 전도도가 높은 타이타늄 실리사이드를 코팅해서 전도도를 높이는 시도를 하였다. 이 합성방법은 실리카에 상온에서 산화타이타늄을 코팅하고 마그네슘 열 환원법을 통해 다공성의 타이타늄 실리사이드가 코팅된 다공성 실리콘을 만들었다. 타이타늄 실리사이드는 리튬과 반응을 하지 않기 때문에 용량 면에서는 손해를 보지만 타이타늄 실리사이드가 코팅된 실리콘은 뛰어난 수명 특성과 출력 특성 뿐 만 아니라 전도도 증가로 인한 전하 전달 저항 감소도 보인다. 이러한 향상된 전기화학 특성은 타이타늄 실리사이드 코팅 때문인데 전도도 증가뿐 아니라

물리적 내구력 또한 뛰어나 수명에 따른 구조 유지에도 도움을 주는 것을 확인 할 수 있다. 대량 생산에 유리한 마그네슘 열 환원법과 전도성과 내구성이 좋은 타이타늄 실리사이드의 결합으로 인한 향상된 전기화학특성은 보이는 이 합성물은 차세대 리튬 이온 전지의 고용량 음극 물질의 후보라고 할 수 있을 것이다.

주요어 : 리튬이온전지, 음극, 실리콘, 마그네슘 열 환원법, 타이타늄 실리사이드

학 번 : 2012-23975